Low-frequency acoustic propagation loss in shallow water over hard-rock seabeds covered by a thin layer of elastic–solid sediment

Steven J. Hughes, Dale D. Ellis, David M. F. Chapman, and Philip R. Staal
Defence Research Establishment Atlantic, P. O. Box 1012, Dartmouth, Nova Scotia B2Y 3Z7, Canada

(Received 11 July 1989; accepted for publication 28 February 1990)

Shallow-water seabeds are often varied and complex, and are known to have a strong effect on acoustic propagation. Some of these seabeds can be modeled successfully as fluid or solid half-spaces. However, unexpectedly high propagation loss with respect to these models has been measured in several regions with rough, partially exposed, hard-rock seabeds. It is shown that the high propagation loss in these areas can be modeled successfully by introducing a thin layer of elastic–solid sediment over the hard-rock substrate. Propagation loss predictions using the SAFARI fast-field program exhibit bands of high loss at regularly spaced frequencies. Normal-mode calculations show resonance phenomena, with large peaks in the modal attenuation coefficients at these same frequencies, and with rapid changes in the mode wavenumbers. Bottom reflection loss calculations indicate that the high propagation loss is due to absorption of shear waves in the sediment layer.

INTRODUCTION

Acoustic propagation in the ocean is influenced by many things. In shallow water, the acoustic field may interact repeatedly with the seabed along the propagation path. Propagation loss is thereby affected strongly by the reflection characteristic of the seabed. Sound energy is lost as a result of radiation into, and absorption by, the seabed, and by scattering at layer boundaries.

The propagation loss characteristics of some seabed types can be modeled by treating the seabed as a fluid or solid half-space substrate, with a plane boundary at the water–substrate interface (Akal and Jensen, 1983). A seabed covered with a thick layer of sediment may be modeled as a fluid half-space, and propagation over a chalk seabed has been treated successfully by including shear-wave conversion and attenuation in the chalk (Ellis and Chapman, 1985). These same models predict low propagation loss over hard-rock seabeds. However, acoustic measurements in several shallow-water areas with partially exposed, hard-rock seabeds, or hard-rock seabeds covered with a thin layer of sediment, reveal very high propagation loss over a wide band of frequencies (MacPherson and Fothergill, 1962; Worley and Walker, 1982; Staal and Chapman, 1985; Beebe and Holland, 1986).

Very little has been published about propagation loss measurements over partially exposed, hard-rock seabeds. MacPherson and Fothergill (1962) show propagation loss measurements from the Hartlen Point region of the Scotian Shelf, an area with a rough, partially exposed, hard-rock seabed. They point out a strong seasonal dependence for the propagation loss, with low propagation loss in the winter, when a positive temperature gradient produces a surface duct, and high propagation loss in summer, when a negative temperature gradient causes the acoustic field to interact with the seabed. Worley and Walker (1982) show data from an experiment in the Gulf of Maine, over a hard-rock seabed with a thin covering of sediment. Their explosive shot data are not calibrated, but the measurements indicate high propagation loss in the area. Beebe and Holland (1986) show propagation loss data from an experiment on the Scotian Shelf, in an area with a thin layer of sediment covering a hard-rock seabed. Their modeling work indicates that neither bottom roughness nor shear-wave excitation in the rock seabed can account for the high acoustic propagation loss below about 100 Hz. They show that the inclusion of a thin layer of solid sediment over the hard-rock substrate can account for the observed propagation loss. Staal and Chapman (1985) present measurements from an experiment on the eastern Canadian Continental Shelf, in an area with a rough, partially exposed, granite seabed. They measured unexpectedly high propagation loss in the 10- to 100-Hz frequency band, and attribute this to seabed roughness. Staal *et al.* (1986) show additional data from the same area, from an experiment designed to determine the effect of bottom roughness on propagation loss over the partially exposed, granite seabed. They determine that although bottom roughness does affect propagation loss, it is not the dominant factor in the high loss observed in the 10- to 100-Hz frequency band. Chamuel and Brooke (1988) present some propagation loss data from the Barrow Strait area, in the Canadian Arctic. Their data display high propagation loss above approximately 10 Hz. They suggest that energy lost to Bragg scattering due to topographical roughness of the seafloor is responsible for the high propagation loss.

Theoretical analyses of the effect of sediment layers on acoustic propagation in the ocean have been presented by Vidmar (1980a,b) and Harrison and Cousins (1985). Harrison and Cousins discuss a number of different sediment and substrate configurations with regard to relative compressional and shear speeds. They state that in the case of a very low shear-speed sediment and a high-speed substrate, one would expect a resonance in the sediment shear wave at a frequency corresponding to a layer thickness of one-quarter wavelength. Vidmar describes the specific case of a layer of solid sediment over a semi-infinite solid substrate. He discusses the conditions for which the sediment layer may be considered thick and treated as a fluid, and contrasts this with the case of a thin layer of sediment, which must be treated as a solid. The sediment layer is thin if the incident compressional wave is able to reach the sediment–substrate interface, where some of the compressional wave energy can be converted into sediment shear-wave energy. He predicts a resonance of the sediment shear wave at frequencies corresponding to a layer thickness of one-quarter wavelength. This sediment shear-wave resonance results in peaks in the bottom reflection loss on the order of 25 dB. He concludes that shear-wave excitation in the thin layer of sediment can be the dominant energy loss mechanism.

The purpose of this work is to show that the high propagation loss measured at some shallow-water sites is due to the excitation of sediment shear waves. We model propagation loss data from five sites: two sites on the Scotian Shelf, one site on the eastern Canadian Continental shelf, one site in the Canadian Arctic, and one site on the UK Continental Shelf. We include new data from an area near one of the sites reported by Beebe and Holland (1986, their site 2), and new data from near the area in Barrow Strait reported by Chamuel and Brooke (1988). Also included are data from the eastern Canadian Continential Shelf reported previously by Staal *et al.* (1986). Except for one of the Scotian Shelf sites and the UK Continental Shelf site, these areas can be characterized by a hard-rock substrate covered by a thin layer of sediment.

In Sec. I, we present theoretical and measured propagation loss over seabeds with three different consolidations: unconsolidated sediment (sand), consolidated sediment (chalk), and hard rock (granite). The theoretical propagation loss data are calculated using the SAFARI program (Schmidt, 1988), a fast-field computer program that implements a full-wave solution of the wave equation for range-independent layered media. We show that the theoretical propagation loss data calculated for a single-layer fluid sand seabed and for a single-layer solid chalk seabed are in agreement with experimental data. For the hard-rock seabed, however, the theoretical propagation loss calculated for the single-layer solid model differs from the experimental data by as much as 60 dB.

In Sec. II, the geoacoustic model for the hard-rock seabed is modified to include an overlaying thin layer of solid sediment. For this two-layer seabed model, we demonstrate that SAFARI, a normal-mode program developed recently at DREA, predicts narrow bands of very high propagation loss, at regularly spaced frequencies. These predictions are in approximate agreement with the experimental propagation loss measurements. Calculations of the mode attenuation coefficients and mode wavenumbers indicate a resonance effect due to the excitation of shear waves in the thin layer of sediment.

In Sec. III, we present calculations of bottom reflection loss for the two-layer seabed model of the site on the eastern Canadian Continental Shelf. Also shown are the components of bottom reflection loss due to absorption of compressional waves and shear waves in the thin layer of sediment, and due to radiation of compressional waves and shear waves into the hard-rock substrate. These calculations indicate that the only significant loss mechanism at the frequencies of high propagation loss is associated with absorption of shear waves in the sediment layer.

Section IV contains a discussion of our results. Particular emphasis is placed on the excitation of shear-wave resonances in the thin layer of sediment. Conclusions are given in Sec. V.

I. EXPERIMENTAL PROPAGATION LOSS AND SIMPLE MODEL

In this section, we present theoretical calculations of acoustic propagation loss as a function of frequency for three different bottom types: unconsolidated sediment (sand), consolidated sediment (chalk), and hard rock (granite). The theoretical propagation loss data are compared with measured data for similar seabeds.

The measured propagation loss data were recorded using the hydrophone array *Hydra* (Staal, 1987). In all cases, explosive charges were used as the acoustic source. The data, taken from hydrophones resting on the seabed, have been averaged over third-octave bands centered at frequencies from 2.5–812.7 Hz.

The theoretical propagation loss data are computed using SAFARI (Schmidt, 1988), a fast-field computer program that calculates acoustic propagation loss in horizontally stratified fluid–solid environments. The program is based on a full-wave solution of the wave equation, and can accommodate a large number of fluid and solid layers. Input to SAFARI consists of a description of the physical environment: the geoacoustic model. The SAFARI geoacoustic model describes each layer in terms of layer thickness, sound speed, attenuation, density, and roughness at the upper boundary of the layer. Shear speed and attenuation are specified for solid layers. Output from SAFARI is coherent propagation loss as a function of range for the given geoacoustic model, source–receiver geometry, and frequency.

The coherent propagation loss output from SAFARI fluctuates rapidly with range. In order to make meaningful comparisons, for a given range, with the measured third-octave propagation loss versus frequency data, it is necessary to smooth out these fluctuations. Smoothed propagation loss versus frequency curves are obtained from the SAFARI output as follows. First, we approximate the propagation loss with a function of the form

$$\mathrm{PL} = A \log(r) + Br + C, \tag{1}$$

where, PL is the approximate propagation loss, r is the source–receiver range, and A, B, and C are constants determined by least-squares techniques. We then sample the approximate propagation loss from Eq. (1) at the range of interest. All theoretical propagation loss calculations presented here from SAFARI make use of Eq. (1).

The simple geoacoustic model is that of a shallow, isovelocity ocean over a semi-infinite seabed. We do not expect exact agreement between the measured data and the results of this model: SAFARI models a continuous source, while the

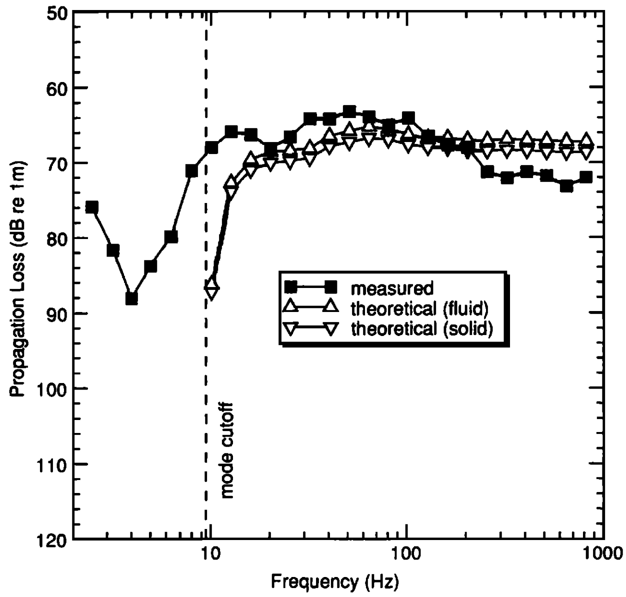

FIG. 1. Measured propagation loss versus frequency over a thick bank of sand (filled squares), and theoretical propagation loss over fluid (upward pointing triangles) and solid (downward pointing triangles) single-layer unconsolidated sediment seabeds (Table I). The source-to-receiver range is 12.7 km; the water depth is 70 m.

experimental data are from an explosive source; the theoretical data do not include the effects of third-octave filtering; SAFARI models a range-independent environment, which is not always a good approximation to the experiment environment; and the model employs an isovelocity sound-speed profile. However, these approximations yield a simple model that is able to show the low-frequency propagation loss features to be illustrated here.

A. Propagation over unconsolidated sediment

Large portions of the Scotian Shelf are made up of sand-covered banks. In areas where the sand is so thick that very little acoustic enegy reaches the substrate, the seabed may be modeled as a fluid half-space (Vidmar, 1980a). In Fig. 1, we show a comparison between measured propagation loss over a thick bank of sand on the Scotian Shelf, and theoretical propagation loss over both fluid and solid half-spaces of sand.

The geoacoustic model for the solid sand seabed is given in Table I. (The geoacoustic model for the fluid seabed is obtained by setting the shear speed and shear attenuation to zero.) The seabed properties are for "Sable Island" sand, a common surficial sediment on the Scotian Shelf. The compressional speed is 1750 m/s (Chapman and Ellis, 1980), the compressional attenuation is 0.26 dB/m/kHz (Dodds, 1980), and the density is 2.06 g/cm^3 (Beebe, 1980). The shear speed and attenuation for the solid seabed are estimated from Hamilton (1980) to be 170 m/s and 13 dB/m/kHz. The sound speed in the water is 1460 m/s, a value typical for winter conditions on the Scotian Shelf. The water depth at the bottom-mounted hydrophone receiver is 70 m, and the acoustic source is a 0.8-kg (1.8-lb) explosive charge detonated at 18.3-m (60-ft) depth. The source-to-receiver range is 12.7 km.

From Fig. 1, we can see that the theoretical propagation loss characteristics for the fluid sand and solid sand seabeds are very similar, with the loss over solid sand about 2 dB greater than over fluid sand. Furthermore, we see that both these theoretical predictions agree well with the measured data at frequencies above the cutoff for nonattenuated modal propagation (about 9.5 Hz) (Urick, 1975). Below 4 Hz, the measured data show energy that may be associated with an interface wave, while the theoretical propagation loss increases dramatically below the mode cutoff frequency. The interface wave would likely propagate along the boundary between the sediment layer and the substrate. With the seabed modeled here by a sand half-space, the boundary between the sediment layer and the substrate has been ignored, so the interface wave effect cannot be predicted.

TABLE I. Geoacoustic model for propagation over an unconsolidated sediment seabed (sand). Sound speed and attenuation in the seabed are given for both compressional waves (p) and shear waves (s).

Layer	Thickness (m)	Sound speed (m/s)	Attenuation (dB/m/kHz)	Density (g/cm^3)
Water	70	1460	0.0	1.0
Seabed	∞	p 1750 s 170	0.26 13.0	2.06

B. Propagation over consolidated sediment

In Fig. 2, we show a comparison between measured propagation loss over a chalk seabed on the UK Continental

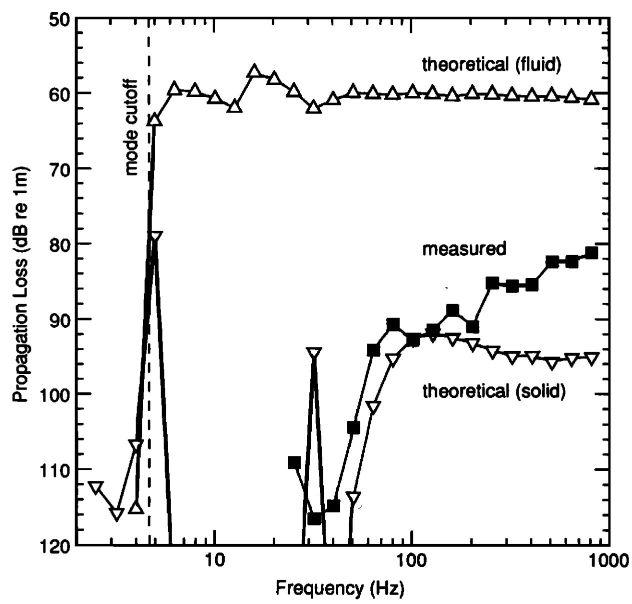

FIG. 2. Measured propagation loss versus frequency over a thick layer of chalk (filled squares), and theoretical propagation loss over fluid (upward pointing triangles) and solid (downward pointing triangles) single-layer consolidated sediment seabeds (Table II). The source-to-receiver range is 13.0 km; the water depth is 106 m.

TABLE II. Geoacoustic model for propagation over a consolidated sediment seabed (chalk). Sound speed and attenuation in the seabed are given for both compressional waves (p) and shear waves (s).

Layer	Thickness (m)	Sound speed (m/s)	Attenuation (dB/m/kHz)	Density (g/cm^3)
Water	106	1500	0.00	1.0
Seabed	∞	p 2400 s 1000	0.1 1.0	2.2

Shelf and theoretical propagation loss over both fluid and solid half-spaces of chalk. The geoacoustic model is given in Table II. (Again, the shear speed and attenuation are set to zero to obtain the geoacoustic model for the fluid seabed.) The compressional speed and attenuation are 2400 m/s and 0.1 dB/m/kHz, the shear speed and attenuation are 1000 m/s and 1.0 dB/m/kHz, and the density is 2.2 g/cm^3 (Ellis and Chapman, 1985). The water sound speed is taken to be 1500 m/s. The water depth at the bottom-mounted hydrophone receiver is 106 m, and the acoustic source is a 0.45-kg (1-lb) explosive charge detonated at 38-m (125-ft) depth. The source-to-receiver range is 13.0 km.

The measured data show high propagation loss below approximately 100 Hz. In contrast, the theoretical data calculated for the fluid seabed show uniform propagation down to the mode cutoff frequency (about 4.7 Hz). The theoretical data calculated for the solid seabed more closely match the measured data, showing high loss at frequencies between 10–100 Hz. We see that it is necessary to include shear-wave conversion in the seabed to predict the propagation loss characteristics measured over the chalk seabed (Staal, 1983; Ellis and Chapman, 1985).

C. Propagation over hard rock

There are extensive shallow-water regions along the east coast of Canada where the seabed was scoured by glaciers during the last ice age. In these areas, the sediment covering is very thin, on the order of a few meters, or nonexistent. There are areas with outcroppings of bedrock, and areas with large boulders scattered about. In Fig. 3, we show a comparison of measured propagation loss over a rough, partially exposed granite seabed off the eastern Canadian Continental Shelf (Staal *et al.*, 1986), and theoretical propagation loss over a solid hard-rock half-space.

The geoacoustic model for the theoretical propagation loss calculations over the solid hard-rock seabed is given in Table III. The sound speed in water is taken to be 1460 m/s, typical for this area. The seabed parameters are for granite (Beebe and Holland, 1986): the compressional sound speed and attenuation are 5500 m/s and 0.1 dB/m/kHz, the shear sound speed and attenuation are 2400 m/s and 0.06 dB/m/kHz, and the density is 2.6 g/cm^3. The water depth at the bottom-mounted hydrophone receiver is 150 m, and the acoustic source is a 0.45-kg (1-lb) explosive charge detonated at 65-m (215-ft) depth. The source-to-receiver range is 13.0 km.

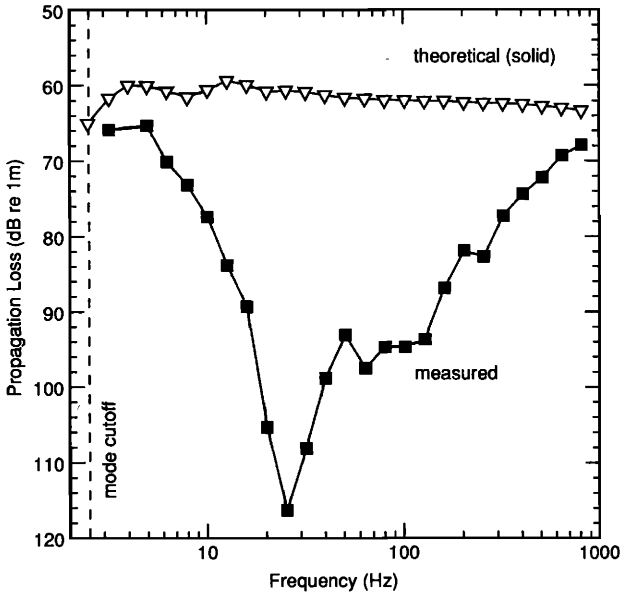

FIG. 3. Measured propagation loss versus frequency over a rough, partially exposed granite seabed (filled squares), and theoretical propagation loss over a single-layer solid, hard-rock seabed (downward pointing triangles) (Table III). The source-to-receiver range is 13.0 km; the water depth is 150 m.

Figure 3 shows clearly that the single-layer solid-seabed model does not account for the propagation loss measured at this site. The measured data exhibit high propagation loss in a wide frequency band below about 1 kHz, while the theoretical calculations predict low propagation loss down to the cutoff frequency for mode 1 (about 2.5 Hz).

In the next section, the geoacoustic model is modified to include a thin layer of solid sediment overlaying the hard-rock substrate. It will be shown that the measured propagation loss curve in Fig. 3, and propagation loss measured at two additional shallow-water sites, can be described successfully by such a model.

II. PROPAGATION LOSS OVER A TWO-LAYER SEABED

In this section, we describe theoretical calculations of propagation loss using a modified model of the seabed: a two-layer model with a thin layer of solid sediment overlaying a hard-rock substrate. The two-layer seabed model yields predictions of bands of very high propagation loss, i.e., propagation nulls, at regularly spaced frequencies.

TABLE III. Geoacoustic model for propagation over an exposed hard-rock seabed (granite). Sound speed and attenuation in the rock seabed are given for both compressional waves (p) and shear waves (s).

Layer	Thickness (m)	Sound speed (m/s)	Attenuation (dB/m/kHz)	Density (g/cm^3)
Water	150	1460	0.00	1.0
Seabed	∞	p 5500 s 2400	0.1 0.06	2.6

TABLE IV. Geoacoustic model for propagation at the Scotian Shelf site. Sound speed and attenuation in the sediment and substrate are given for both compressional waves (p) and shear waves (s).

Layer	Thickness (m)	Sound speed (m/s)	Attenuation (dB/m/kHz)	Density (g/cm^3)
Water	72	1460	0.00	1.0
Sediment	5	p 1780 s 170	0.7 13.0	2.2
Substrate	∞	p 5500 s 2400	0.1 0.06	2.6

TABLE VI. Geoacoustic model for propagation at the Arctic Shelf site. Sound speed and attenuation in the sediment and the rock substrate are given for both compressional waves (p) and shear waves (s).

Layer	Thickness (m)	Sound speed (m/s)	Attenuation (dB/m/kHz)	Density (g/cm^3)
Water	165	1460	0.00	1.0
Sediment	2.5	p 2000 s 800	0.15 1.75	2.1
Substrate	∞	p 5500 s 2400	0.1 0.06	2.6

A. The geoacoustic model

The geoacoustic models for three shallow-water sites with sediment-covered hard-rock seabeds (Scotian Shelf, Continental Shelf, and Arctic Shelf) are given in Tables IV–VI. At two sites (Scotian Shelf and Continental Shelf), the thin layer of sediment is composed of sand, with low shear speed and high shear attenuation. At the third site (Arctic Shelf), the thin layer is composed of glacial till, with a higher shear speed and lower attenuation. At all three sites, the underlying hard-rock substrate has high speed and low attenuation for both compressional and shear waves.

The first site (Scotian Shelf, Table IV) is modeled by a 5-m layer of low shear-speed sand covering a granite substrate. The layer thickness and geoacoustic parameters for the sediment are from Beebe and Holland (1986): the compressional sound speed and attenuation are 1780 m/s and 0.7 dB/m/kHz, the shear sound speed and attenuation are 170 m/s and 13 dB/m/kHz, and the density is 2.2 g/cm^3. Also from Beebe and Holland (1986) are the geoacoustic parameters for the granite substrate: the compressional sound speed and attenuation are 5500 m/s and 0.1 dB/m/kHz, the shear sound speed and attenuation are 2400 m/s and 0.06 dB/m/kHz, and the density is 2.6 g/cm^3. The sound speed in water is taken to be 1460 m/s. The water depth at the bottom-mounted hydrophone receiver is 72 m, and the acoustic source is a 0.8-kg (1.8-lb) explosive charge detonated at 18.3-m (60-ft) depth. The source-to-receiver range is 12.4 km.

The second site (Continental Shelf, Table V) is modeled using the same sediment and substrate parameters as specified for the Scotian Shelf site (Table IV), except that the thickness of the sediment layer is 1.75 m. The thickness of the sediment layer has been chosen to position the null in the theoretical propagation loss at the experimentally observed null frequency of about 25 Hz. The remaining geoacoustic parameters are the same as given above in Sec. I C (Table III) for the Continental Shelf site.

TABLE V. Geoacoustic model for propagation at the Continental Shelf site. Sound speed and attenuation in the sediment and the rock substrate are given for both compressional waves (p) and shear waves (s).

Layer	Thickness (m)	Sound speed (m/s)	Attenuation (dB/m/kHz)	Density (g/cm^3)
Water	150	1460	0.00	1.0
Sediment	1.75	p 1780 s 170	0.7 13.0	2.2
Substrate	∞	p 5500 s 2400	0.1 0.06	2.6

The third site (Arctic Shelf, Table VI) is modeled by a 2.5-m-thick layer of glacial till with the following geoacoustic parameters: the compressional sound speed and attenuation are 2000 m/s and 0.15 dB/m/kHz, the shear sound speed and attenuation are 800 m/s and 1.75 dB/m/kHz, and the density is 2.1 g/cm^3. The compressional sound speed is based on field observations (Ozard, 1989), while the other parameters are estimates based on the structure of the till material. The thickness of the till layer is consistent with field observations in the area (Ozard, 1989), and has been chosen to produce a null in the theoretical data at the observed null frequency of about 130 Hz. The sound speed in water is taken to be 1460 m/s. The water depth at the bottom-mounted hydrophone receiver is 165 m, and the acoustic source is a 0.45-kg (1-lb) explosive charge detonated at 65-m (215-ft) depth. The source-to-receiver range is 9.3 km.

B. SAFARI propagation loss calculations

Using the SAFARI program, theoretical propagation loss data have been calculated for the shallow-water sites described above and specified by the geoacoustic models given in Tables IV–VI. Figures 4–6 show the theoretical and measured propagation loss data for each site. In all cases, the measured data exhibit high loss across a wide band of frequencies.

Figure 4 shows a comparison between measured propagation loss at the Scotian Shelf site and theoretical propagaton loss for the two-layer seabed model given in Table IV. Also shown are the data of Beebe and Holland (1986). Their data were obtained in only 32 m of water and at a source–receiver range of just 4 km. Our measured propagation loss data from a nearby site are nonetheless very similar, and are extended in frequency down to 2.5 Hz. The measured propagation loss increases steadily with decreasing frequency from 1 kHz down to about 80 Hz. Below 6 Hz, there is evi-

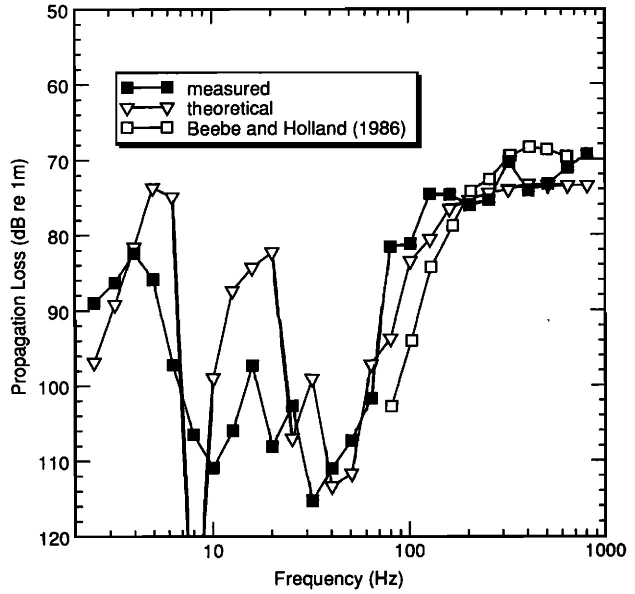

FIG. 4. Measured propagation loss versus frequency at the Scotian Shelf site (filled squares), and theoretical propagation loss for the corresponding two-layer seabed (downward pointing triangles) (Table IV). The source-to-receiver range is 12.4 km; the water depth is 72 m. Also shown, for comparison, are Beebe and Holland's data (1986) (open squares).

dence in the measured data of an interface wave, probably propagating along the sediment–substrate interface. The theoretical propagation data match the measured data well above 40 Hz. There is also an indication in the theoretical data of an interface wave at 5 Hz. Note the peaks (bands of low propagation loss at 4, 16, and 25 Hz) and nulls (bands of high propagation loss at 10, 20, and 32 Hz) in the measured propagation loss, and corresponding peaks (at 5, 20, and 32 Hz) and nulls (at 8, 25, and 40 Hz) in the theoretical propagation loss data. These peaks and nulls are evidence of a resonance condition associated with the thin layer of solid sediment, and will be discussed in some detail in Sec. III.

The propagation loss data measured at the Continental Shelf site, previously reported by Staal *et al.* (1986), are shown in Fig. 5 with the theoretical calculation of propagation loss using the two-layer seabed model given in Table V. The measured propagation loss increases steadily with decreasing frequency from 1 kHz down to about 50 Hz, with a band of very high propagation loss centered at 25 Hz. Below 25 Hz, the propagation loss decreases rapidly to a minimum at 5 Hz. The theoretical propagation loss data show a deep primary null at 25 Hz and a secondary null at about 70 Hz. These nulls are evidence of a resonance condition associated with the thin layer of solid sediment.

The measured and theortical propagation loss data for the Arctic Shelf site are shown in Fig. 6. The measured propagation loss is reasonably constant from 1 kHz down to about 15 Hz, with the exception of a null at about 130 Hz. Below 15 Hz, the propagation loss decreases, probably due to an interface wave and low-order modes. The theoretical propagation loss data match the measured data well at and above the null at 130 Hz, and below about 10 Hz. Between these frequencies, the theoretical propagation loss is much less than the measured propagation loss. This discrepancy is likely due to the approximations made in the modeling and an incomplete knowledge of the seabed structure at the experimental site. Even so, the propagation null at 130 Hz is

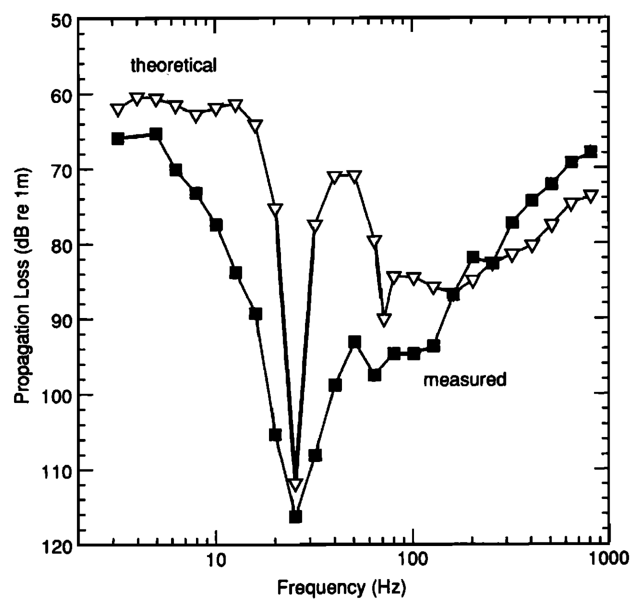

FIG. 5. Measured propagation loss versus frequency at the Continental Shelf site (filled squares), and theoretical propagation loss for the corresponding two-layer seabed (downward pointing triangles) (Table V). The source-to-receiver range is 13.0 km; the water depth is 150 m.

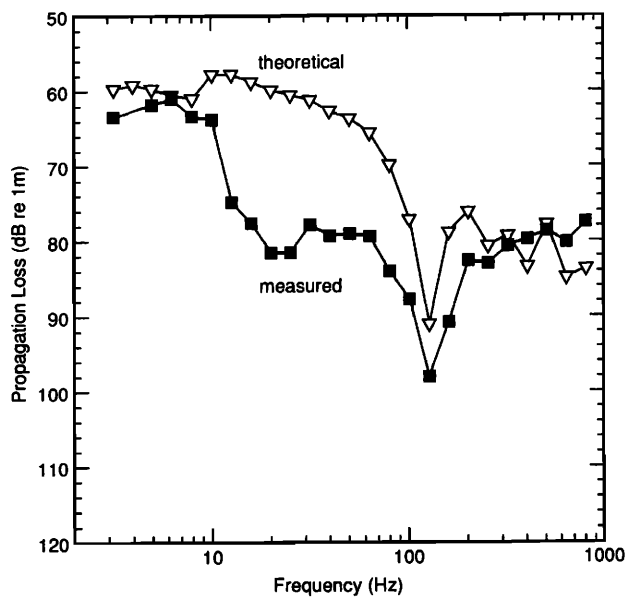

FIG. 6. Measured propagation loss versus frequency at the Arctic Shelf site (filled squares), and theoretical propagation loss for the corresponding two-layer seabed (downward pointing triangles) (Table VI). The source-to-receiver range is 9.3 km; the water depth is 165 m.

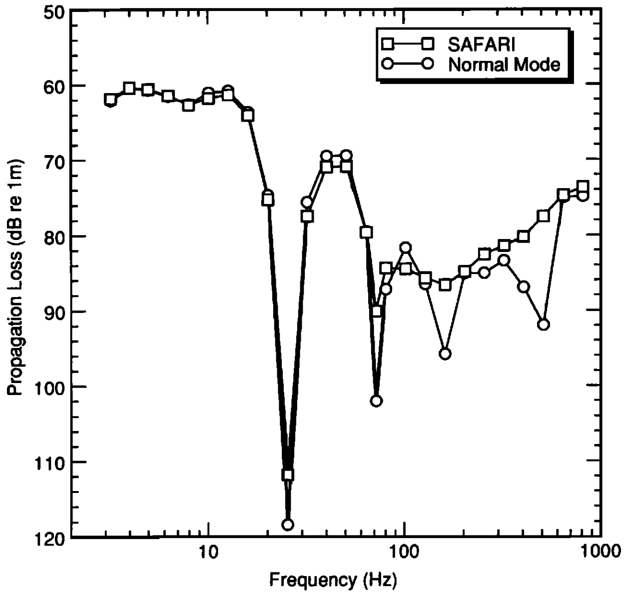

FIG. 7. Theoretical propagation loss versus frequency for the two-layer seabed model for the Continental Shelf site (Table V), using the SAFARI program (open squares) and the DREA normal-mode program (open circles). The source-to-receiver range is 13.0 km; the water depth is 150 m.

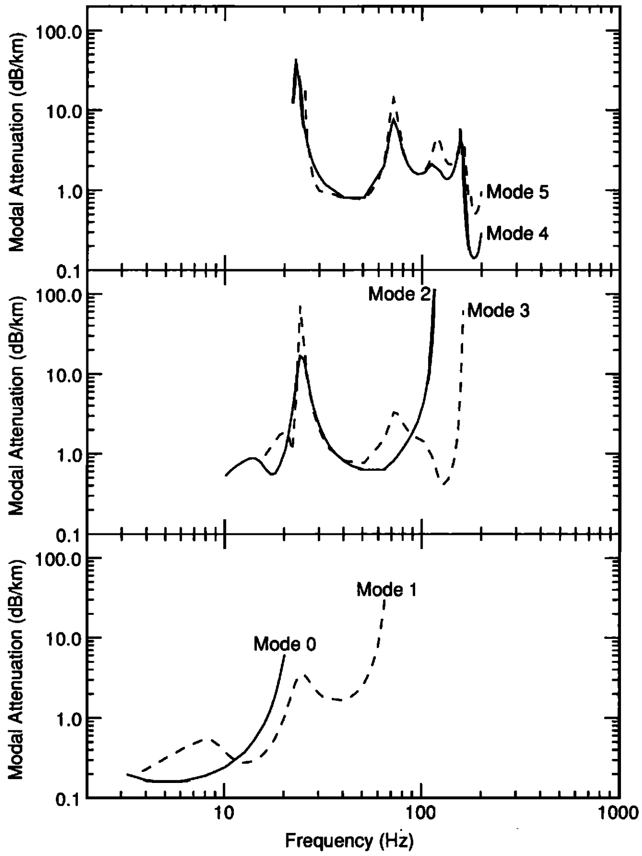

FIG. 8. Normal-mode attenuation coefficients versus frequency for the first six modes ($n = 0$ to 5), based on the geoacoustic model for the Continental Shelf site (Table V). Note that the lowest-order mode drops out as the frequency increases through each resonance.

strong, and is evidence of a resonance in the thin layer of glacial till.

C. Normal-mode calculations

A normal-mode program has been developed using a generalization of the method of Hall *et al.* (1983) to obtain the mode wavenumbers and mode functions for an environment with multiple solid layers. Mode normalizations, attenuations, and group velocities are then obtained using the formulas of Koch *et al.* (1983). The model is discussed in more detail in Appendix A. Propagation loss calculations, performed for the Continental Shelf case using the inputs from Table V (source–receiver range is 13.0 km), are compared with the SAFARI predictions in Fig. 7. The normal-mode propagation loss predictions are made by summing the modes incoherently, while the SAFARI predictions are obtained from smoothing the coherent propagation loss output using Eq. (1). In spite of the differences between the two calculations, the predictions are in excellent agreement up to about 100 Hz. Above 100 Hz, the two models are in reasonable agreement, although the normal-mode calculations show nulls that are not present in the SAFARI predictions. Calculations of mode attenuations and eigenvalues are also presented below, since they help explain the nature of the resonances at low frequencies.

Figure 8 shows attenuation coefficents in dB/km for the first few modes. Note the very high attenuations around 25 and 70 Hz, corresponding to the high loss bands in the measured propagation loss and in the model predictions shown in Figs. 5 and 7. These result from resonances in the thin layer of sediment, at frequencies corresponding to 1/4 and 3/4 wavelengths of the shear wave. Since the measured data shown in Fig. 5 are averaged over third-octave bands, the effect of the resonances at higher frequencies is reduced in the measurements compared to the model predictions. Another interesting feature of the modal attenuation coefficients, not evident from Fig. 8, is that at the higher frequencies the attenuation coefficients are relatively large for modes corresponding to grazing angles around 30° in the water. This behavior corresponds to the plane-wave reflection loss results described in the next section [and illustrated in Fig. 10(a)]. Also, the attenuation is quite low at angles just below the critical angle, or mode cutoff; this means that it is essential to include both the low-order modes and the high-order modes in the propagation loss calculations.

Group velocity calculations are not presented here, but they often show minima at the frequencies corresponding to the attenuation peaks. This is expected since the formula for the group velocity is identical to the formula for the modal attenuation coefficient when the absorption coefficients are replaced by the reciprocal of the corresponding sound speeds [see Eqs. (A14) and (A15)].

The mode eigenvalues are also interesting, since the thin layer of sediment has a dramatic effect on them. Instead of looking at the usual mode phase velocities or horizontal wavenumber κ_n, we look at the vertical wavenumber γ_n, in the water:

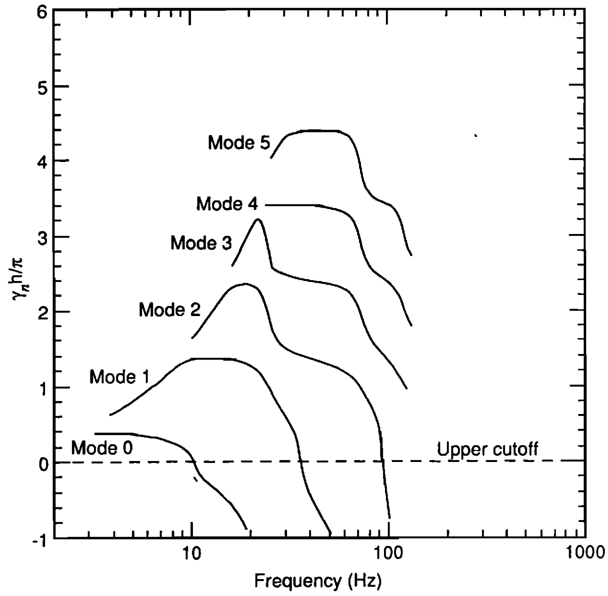

FIG. 9. Normal-mode eigenvalues, $\gamma_n h/\pi$ versus frequency for the first six modes ($n = 0$ to 5), based on the geoacoustic model for the Continental Shelf site (Table V). Note the rapid change (by π) near each resonance, and the plateaus at half-integer multiples of π between resonances.

$$\gamma_n = (\omega^2/c_w^2 - \kappa_n^2)^{1/2}, \tag{2}$$

where ω is the frequency, and c_w the sound speed in the water. There are several reasons for using the vertical wavenumber. Since the sound speed in the water is constant for our calculations, the mode functions are described simply by $A_n \sin(\gamma_n z)$, where z is the depth coordinate measured from the sea surface, and A_n is the mode normalization constant. The phase of the mode function at the seabed ($z = h$) is determined by $\gamma_n h$, and the relative amplitude by $\sin(\gamma_n h)$. Figure 9 shows $\gamma_n h/\pi$ as a function of frequency for the first few modes. Of particular interest is the fact that, for a given mode, $\gamma_n h$ is relatively constant for frequencies between the resonances, but drops by π as the frequency increases through a resonance. The resonance corresponds to $\gamma_n h$ being a multiple of π. In the absence of a thin layer, $\gamma_n h$ would start just above $(n - 1/2)\pi$ at the mode cutoff frequency, rise toward $(n + 1/2)\pi$ as the frequency increases, then drop slowly toward, but never cross, $n\pi$ as the frequency increases without bound. (Mode 0 is somewhat unique: $\gamma_0 h$ would start at 0, rather than $-\pi/2$, increase toward $\pi/2$, then decrease through 0, at which point $\gamma_0 h$ would become imaginary corresponding to the mode becoming an interface wave.) However, when the thin layer is present, $\gamma_n h$ drops by π as the frequency increases through a resonance. Thus mode n changes its character and begins to look like mode $(n-1)$ since $\sin(\gamma_n z)$ then has one fewer zero crossing in the water. For example, at the first resonance (about 25 Hz), mode 0 starts to look like an interface wave and mode 1 starts to look like a zero-order mode. At the second resonance (about 70 Hz), all the modes lose another zero crossing in the water column, and mode 1 becomes an interface wave as well. The disappearance of the zero crossing in the water column is compensated for by the additional zero crossing (of the shear-wave component of the mode function) in the thin layer of sediment. Since the interfacial modes are highly attenuated, this in some sense gives the modes an upper cutoff frequency; cf. Figs. 8 and 9. The positions of the resonances are determined by the thickness of the layer and the low shear speed in that layer. For example, if the thickness of the thin layer were increased by 50% (less than 1 m), the resonances would be moved to 16, 48, 80 Hz, etc. The presence of a thin layer can have a dramatic effect on the propagation.

III. BOTTOM REFLECTION LOSS

Acoustic propagation loss in shallow water is affected strongly by reflection loss at the seabed. It is instructive, therefore, to calculate bottom reflection loss for the two-layer seabed model, where both layers support shear waves. It is also instructive, in this case, to calculate that portion of the acoustic energy incident on the seabed that is lost due to refraction into a given layer of the seabed. Based on Brekhovskikh's work describing the calculation of reflection and transmission coefficients for multilayered media (Brekhovskikh, 1980), we have calculated total bottom reflection loss and reflection loss due to excitation and absorption of compressional waves and shear waves in the two seabed layers. Details of these calculations are given in Appendix B.

Calculations of theoretical bottom reflection loss for the Continental Shelf site (Table V) are shown in Fig. 10(a)–(e). These data are shown as grey-scale plots, calculated for grazing angles from 0° to 90°, and for frequencies from 2 to 1024 Hz. The data are plotted in terms of energy loss with respect to an incident plane wave in the water layer. The scales are full white for low loss (0 dB), and full black for high loss (16 dB or more). Note that the total bottom reflection loss [Fig. 10(a)] is the sum of the components of reflection loss [Fig. 10(b)–(e)] due to absorption and radiation in the seabed layers. However, since the density scale is not linear and the grey levels are quantized to the nearest integral decibel value, the appearance of the total bottom reflection loss plot may be deceiving. In particular, it is possible for the total bottom loss figure to indicate greater loss then one would expect from the component figures. Each of the figures is described below.

Figure 10(a) shows the total theoretical bottom reflection loss for the seabed at the Continental Shelf site. The figure shows, for a given frequency and grazing angle, the energy lost from the water layer into the seabed. High loss, full black in the figure, means that very little energy is reflected back into the water layer, while low loss means that very little energy is lost into the seabed. At zero grazing angle, there is total reflection back into the water, and the figure shows full white for all frequencies. There is little bottom loss at low frequencies and low grazing angles. This is consistent with the low propagation loss measured in this frequency band at this site. At grazing angles greater than about 52°, the critical angle for shear waves in the substrate, there is relatively high bottom reflection loss, particularly at higher frequencies. At certain frequencies (near 25, 70, 130 Hz, etc.), the figure shows high loss over a wide range of grazing angles. At these frequencies, one would expect high

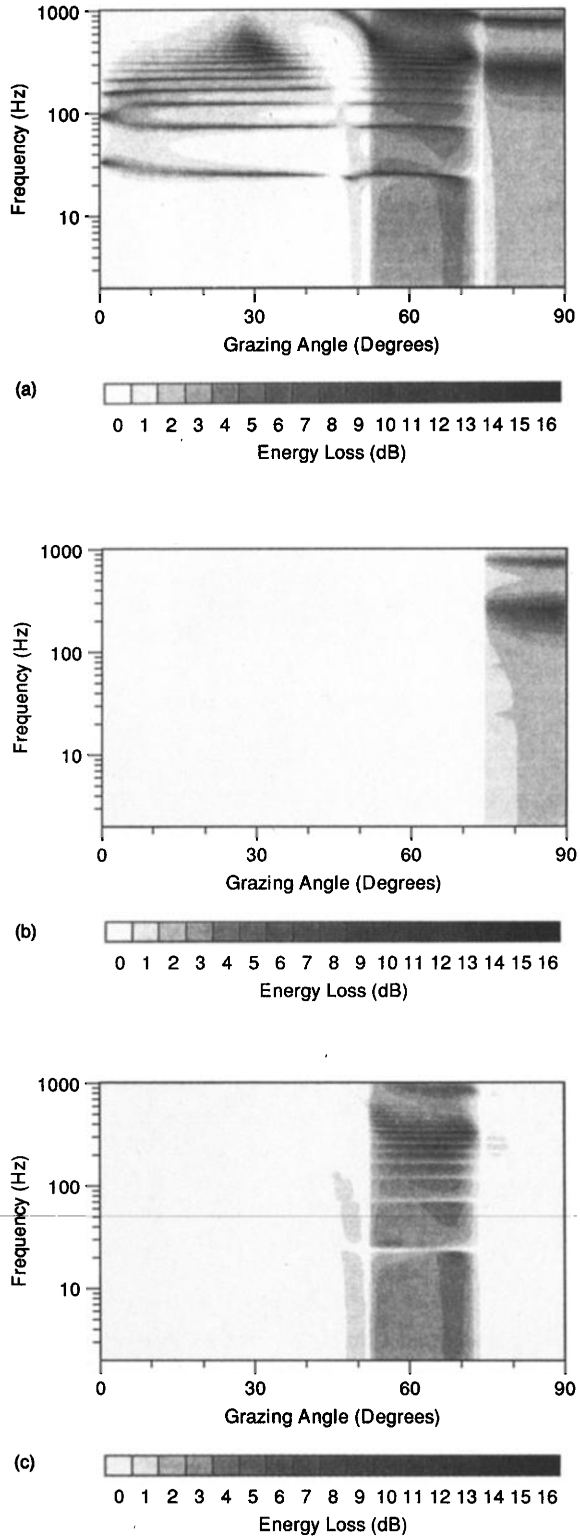

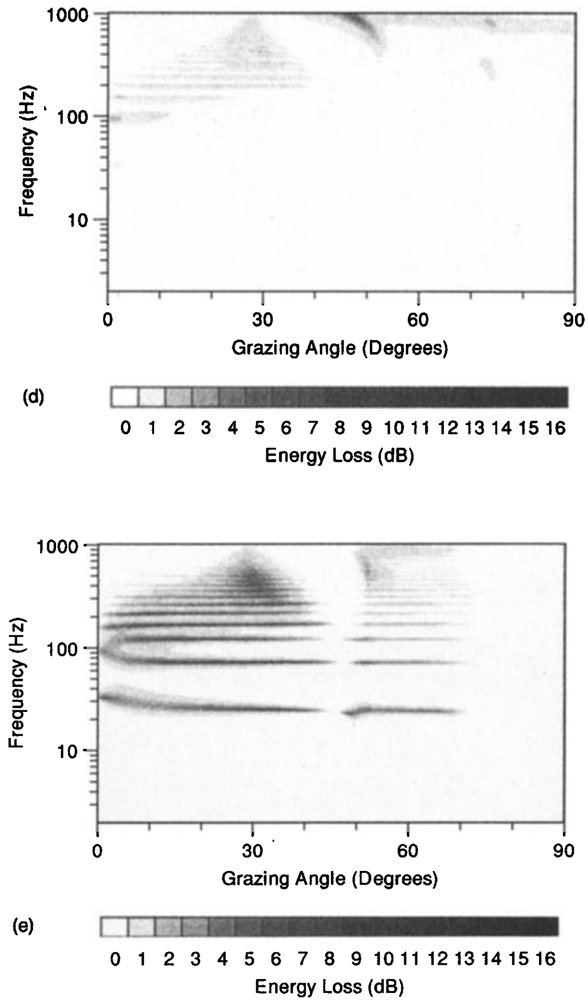

FIG. 10. (a) Total bottom reflection loss versus frequency and grazing angle based on the geoacoustic model of the Continental Shelf site (Table V). Note the high bottom reflection loss for a wide range of grazing angles at frequencies corresponding to the propagation nulls (bands of very high propagation loss at 25 Hz, 70 Hz, etc.) shown in Fig. 5. (b) The component of bottom reflection loss due to radiation of compressional waves into the substrate for the two-layer seabed model for the Continental Shelf site (Table V). The critical angle for compressional waves in the substrate is about 75°. (c) The component of bottom reflection loss due to radiation of shear waves into the substrate for the two-layer seabed model for the Continental Shelf site (Table V). The critical angle for shear waves in the substrate is about 52°. (d) The component of bottom reflection loss due to absorption of compressional waves in the thin layer for the two-layer seabed model for the Continental Shelf site (Table V). (e) The component of bottom reflection loss due to absorption of shear waves in the thin layer for the two-layer seabed model for the Continental Shelf site (Table V). Note the high bottom loss for a wide range of grazing angles at frequencies corresponding to the propagation nulls.

propagation loss over this seabed, as has been found to be the case for the Continental Shelf (see Fig. 5). At higher frequencies, as the sediment layer becomes acoustically thick, the effect of the bottom structure becomes less pronounced, and the angular range of high reflection loss decreases to a narrow band of grazing angles about 30°. This is consistent with large attenuation coefficients for modes at this grazing angle, as discussed in Sec. II C.

Figure 10(b) shows the component of bottom reflection loss due to the radiation of compressional waves into the hard-rock substrate. The figure shows clearly that the only significant loss here occurs at grazing angles above the critical angle of 75°.

Figure 10(c) shows the component of bottom reflection loss due to radiation of shear waves into the hard-rock substrate. This figure shows that a significant contribution to the bottom reflection loss occurs in a band of grazing angles delineated by the critical angle for shear waves in the substrate of 52°, and the critical angle for compressional waves in the substrate of 75°. The white horizontal features at the frequencies of the propagation nulls (near 25, 70, 130 Hz, etc.), indicate that there is little acoustic energy in the substrate shear wave at these frequencies. There is also a contribution to the bottom reflection loss at a grazing angle of about 50° and for frequencies below about 100 Hz. This loss component below the critical angle is due to the finite attenuation of shear waves in the substrate.

Figure 10(d) shows the component of bottom reflection loss due to the absorption of compressional wave energy in the thin layer of sediment. At frequencies below a few hundred hertz, there is very little bottom reflection loss due to absorption of the compressional wave in the sediment layer. At higher frequencies, where the sediment layer becomes acoustically thick, there is a small component of the bottom reflection loss due to absorption of compressional waves in the sediment layer.

Finally, Fig. 10(e) shows the component of bottom reflection loss due to the absorption of shear-wave energy in the thin layer of sediment. This figure shows that there is little bottom loss due to sediment shear-wave absorption at frequencies other than those of the propagation nulls. At these frequencies, this component of the bottom loss extends over a wide range of grazing angles. This indicates that the high propagation loss at these frequencies is due to the excitation and absorption of shear waves in the thin layer of sediment.

IV. DISCUSSION

We have shown that a single-layer seabed model, using a fluid or solid-half-space seabed, is inadequate for predicting the acoustic propagation loss measured over partially exposed, hard-rock seabeds. The single-layer model predicts low propagation loss, whereas we have measured high propagation loss over a wide band of frequencies at three different shallow-water sites. We have shown that some of the measured propagation loss features can be modeled successfully by including a thin layer of solid sediment over the hard-rock substrate. In particular, this two-layer seabed model predicts narrow bands of very high propagation loss that approximate the observed propagation loss characteristics.

A detailed theoretical explanation of the sediment shear-wave resonance mechanism has been given by Vidmar (1980a,b). In the present context, it appears as though the compressional wave incident from the water passes through the sediment layer to the substrate. Since the sediment layer is thin, the incident compressional wave suffers little attenuation, and is partially converted to a sediment shear wave at the sediment–substrate interface. The sediment shear speed is small, so the sediment shear wave travels almost vertically for any angle of incidence of the compressional wave in the water. A resonance condition exists when the thickness of the sediment layer is an odd multiple of quarter wavelengths of the shear wave. The sediment shear wave is attenuated highly, and, at resonance, sediment shear-wave excitation is the dominant energy-loss mechanism.

At low frequencies, the reflection and transmission coefficients for the seabed layers are controled by the properties of the shear wave in the sediment layer. The resonance condition is satisfied when

$$\kappa d = m\pi/2 \quad (m = 1,3,5,...), \tag{3}$$

where κ is the wavenumber ($\kappa = 2\pi/\lambda$), d is the sediment thickness, and m is an odd integer. At resonance, most of the incident acoustic energy is absorbed via the sediment shear wave. Since this happens over a wide range of grazing angles, there is very high acoustic propagation loss at these frequencies. At higher frequencies, the reflection and transmission coefficients are increasingly more dependent on the behavior of the compressional wave in the sediment, and the effect of the shear-wave resonance diminishes. This is manifested in better propagation at higher frequencies. In the limit of very high frequencies, the sediment layer becomes thick in the sense that the incident compressional wave is greatly attenuated by the time it encounters the sediment–substrate interface, and very little energy is converted into the sediment shear wave. In this regime, the seabed may be modeled as a semi-infinite fluid (Vidmar, 1980a). It is interesting to note that the sediment layer becomes nearly transparent, except for small compressional wave losses, at wavelengths for which κd is an integral multiple of π.

It is beyond the scope of this paper to deal with the mode functions in any great detail, but the essential feature of the resonance is that all the mode functions tend to be small at the bottom of the water column when the frequency is close to a resonance, since $\gamma_n h$ is near a multiple of π. As well, the amplitude of the vector potential in the thin layer is relatively large at these frequencies. This is analogous to the resonance effects in the mode functions and group velocities discussed by Chapman and Ellis (1983) for fluid sediments. All the modes reach resonance at the same frequency, due to the fact that the shear speed is so low in the sediment layer; so for all angles of incidence (mode arrival angles in the water), the shear-wave component in the sediment is traveling nearly vertically.

Other researchers have presented different hypotheses to explain the very high propagation loss characteristics presented here. Staal and Chapman (1985) suggested that roughness at the substrate interface could cause bulk scattering that would result in higher propagation loss. However, Staal *et al.* (1986) describe an experiment, at the same site, that shows the high loss centered at about 25 Hz to be largely independent of seabed topography. The effect of interface roughness on the theoretical propagation loss has been calculated using a recent version of the SAFARI program (Kuperman and Schmidt, 1986), which can include interface roughness in its geoacoustic model. Figure 11 shows a comparison of theoretical propagation loss over a smooth granite seabed and over a rough granite seabed. The seabed is modeled as a semi-infinite solid using the substrate parameters given in Table V. The interface roughness is 4.9 m (rms), measured acoustically at the experiment site. This roughness value compares well with values reported elsewhere for similar areas (Berkson and Matthews, 1983). Figure 11 shows that interface roughness has a strong effect on propagation

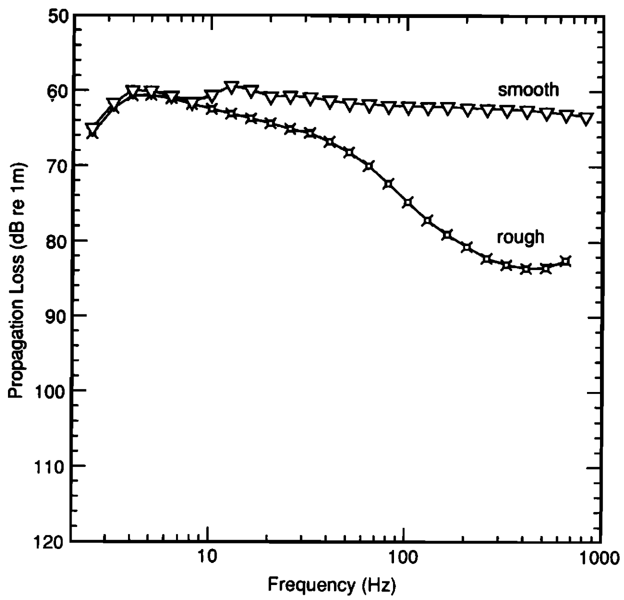

FIG. 11. Theoretical propagation loss versus frequency over a smooth granite seabed (downward pointing triangles) (Table III), and over a rough granite seabed (open stars) (4.9 m rms roughness).

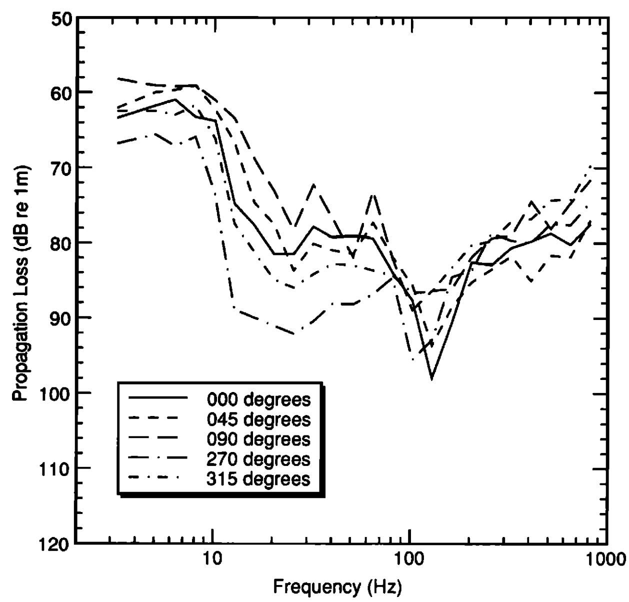

FIG. 12. Measured propagation loss versus frequency at the Arctic Shelf site, for a range of bearing angles. Note the high propagation loss above about 20 Hz is evident for all bearing angles.

loss at higher frequencies (above 100 Hz), but does not produce the deep null that has been measured in the 10- to 100-Hz frequency band. This is consistent with, and supports, the experimental findings of Staal *et al.* (1986).

Chamuel and Brooke (1988) suggest that energy losses, due to Bragg scattering, associated with interface roughness may be responsible for the high propagation loss they observed above approximately 10 Hz. Our data from the same area in the Canadian Arctic, shown in Fig. 12, do not support this argument. The figure shows propagation loss recorded for a series of explosive charges detonated in a circle around an array of bottom mounted hydrophones. The figure shows measured propagation loss versus frequency at one of the hydrophones for various bearing angles around the array. Any propagation loss characteristic dependent upon Bragg scattering would exhibit an angular dependence: i.e., show high propagation loss along one direction and low propagation loss along the perpendicular direction. The data do not show this characteristic, rather, they show an increase in the propagation loss above 10 Hz for all directions. This behavior is consistent with the effect of a thin layer of sediment (glacial till) overlaying a hard-rock seabed.

V. CONCLUSIONS

We have shown typical characteristics for acoustic propagation loss in shallow water over three seabed types: unconsolidated sediment (sand), consolidated sediment (chalk), and hard rock (granite). For propagation over unconsolidated sediment, the seabed can be modeled as a semi-infinite fluid, and a consolidated sediment seabed can be modeled as a semi-infinite solid. These simple single-layer seabed models predict low propagation loss over a hard-rock seabed. However, at several sites with rough partially exposed granite seabeds, we have measured high propagation loss over a wide band of frequencies. We have shown that this type of seabed may be modeled successfully by including a thin layer of solid sediment in the geoacoustic model. This two-layer seabed model predicts narrow bands of very high propagation loss that approximate the observed propagation loss characteristics.

We have shown that the observed high propagation losses are associated with sediment shear-wave resonances within the layer of sediment. The dominant loss mechanism at low frequencies is excitation of shear waves in the layer, and the sediment layer can have profound effect on the low-frequency acoustic propagation loss characteristics. We expect other areas with thin layers of sediment covering hard-rock seabeds to have similar propagation loss characteristics.

APPENDIX A: NORMAL-MODE CALCULATIONS

Here, we sketch out the equations and method used to perform the normal-mode calculations. The normal-mode equations and expressions for the mode normalizations and attenuation are taken from Koch *et al.* (1983). The numerical solution is expressed in matrix form as a generalization of the technique of Hall *et al.* (1983) to solid layers; standard numerical packages are used to solve for the mode eigenvalues and mode functions.

The environment consists of N horizontally stratified layers, each of which may have elastic properties. Each layer is characterized by a thickness h, density ρ, compressional sound speed c_p, compressional attenuation coefficient ε_p, and for the solid layers a shear sound speed c_s and attenuation coefficient ε_s. Within each layer, the depth-dependent parts of the scalar and vector displacement potentials, u_n and v_n, respectively, for mode n are given by

$$u_n'' + (\omega^2/c_{pj}^2 - \kappa_n^2) u_n(z) = 0 \tag{A1}$$

and

$$v_n'' + (\omega^2/c_{sj}^2 - \kappa_n^2) v_n(z) = 0, \tag{A2}$$

where the additional subscript j refers to layer j, κ_n is the horizontal wavenumber for the nth mode, and the primes refer to derivatives with respect to the depth coordinate z. At interfaces between the layers, a number of continuity conditions apply:

$$u_n' + \kappa_n^2 v_n, \tag{A3}$$

$$\rho u_n - 2(\kappa_n^2/\kappa_s^2)(u_n + v_n'), \tag{A4}$$

$$2u_n' + (2\kappa_n^2 - \kappa_s^2) v_n, \tag{A5}$$

$$\rho(u_n + v_n'). \tag{A6}$$

In the above equations, $\kappa_s = \omega/c_s$. These conditions follow from the continuity of vertical particle displacement, continuity of normal stress $\mathscr{T}_{zz}$, continuity of tangential stress $\mathscr{T}_{rz}$, and continuity of radial particle displacement. All four conditions apply at a solid–solid interface; at a fluid–solid interface, the first three apply, and $\mathscr{T}_{rz} = 0$ in the fluid; at a fluid–fluid interface, only the first two conditions apply (with $v_n \equiv 0$, of course).

Within each layer, the solution can be written in terms of two independent solutions $f(z)$ and $g(z)$:

$$u_n(z) = A_j f_{pj}(z) + B_j g_{pj}(z) \tag{A7}$$

and

$$v_n(z) = C_j f_{sj}(z) + D_j g_{sj}(z), \tag{A8}$$

where the subscript j refers to the layer, and p and s refer to the compressional and shear components. In our case, the layers have constant sound speeds, so the functions f and g are either $\sin(\gamma z)$ and $\cos(\gamma z)$, or $\exp(-|\gamma| z)$ and $\exp(|\gamma| z)$, where $\gamma = (\omega^2/c^2 - \kappa_n^2)^{1/2}$. The choice of functions depends on whether γ is real or imaginary.

Fairly general boundary conditions of the form $au_n + bu_n' = 0$ can be allowed. For the calculations described in this paper, the following conditions have been used:

at the ocean surface

$$u_n(0) = 0; \tag{A9}$$

at the top of the bottom most layer

$$u_n'(z_N) = (\kappa_n^2 - \omega^2/c_{pN}^2)^{1/2} u_n(z_N) \tag{A10}$$

and

$$v_n'(z_N) = (\kappa_n^2 - \omega^2/c_{sN}^2)^{1/2} v_n(z_N). \tag{A11}$$

The solution can now be reduced to the solution of a matrix equation. Equation (A12) illustrates the form of the equation for the fluid–solid–solid case modeled in this paper. Many of the matrix elements are zero, as shown. The lower case x's represent terms of the matrix that are nonzero (but not, in general, equal to one another); the uppercase X's mark the diagonal, but similarly have no other particular numerical significance.

$$\begin{bmatrix} X & x & 0 & 0 & 0 & 0 & 0 & 0 & 0 & 0 \\ x & X & x & x & x & x & 0 & 0 & 0 & 0 \\ x & x & X & x & x & x & 0 & 0 & 0 & 0 \\ x & x & x & X & x & x & 0 & 0 & 0 & 0 \\ 0 & 0 & x & x & X & x & x & x & x & x \\ 0 & 0 & x & x & x & X & x & x & x & x \\ 0 & 0 & x & x & x & x & X & x & x & x \\ 0 & 0 & x & x & x & x & x & X & x & x \\ 0 & 0 & 0 & 0 & 0 & 0 & x & Y & X & x \\ 0 & 0 & 0 & 0 & 0 & 0 & x & x & x & Y \end{bmatrix} \begin{bmatrix} A_1 \\ B_1 \\ A_2 \\ B_2 \\ C_2 \\ D_2 \\ A_3 \\ B_3 \\ C_3 \\ D_3 \end{bmatrix} = 0. \tag{A12}$$

There are ten equations: one for the surface boundary condition, three for the fluid–solid interface, four for the solid–solid interface, and two for the basement boundary conditions on the scalar and vector potentials. The Y's in the last two rows represent the only nonzero elements when the basement boundary represents a half-space with decaying exponential solutions, as in Eqs. (A10) and (A11).

The eigenvalues are obtained using a generalization of the method of Hall *et al.* (1983) to handle solid layers. They construct a matrix like the one shown in Eq. (A12), and find the zeros of a determinant. Our code uses the banded matrix solver SGBDI from the LINPACK linear algebra package (Dongarra *et al.*, 1979) to obtain the determinant, and the IMSL (1982) root finder ZBRENT to obtain the zeros. The determinant undergoes large positive and negative excursions; for thick layers and high frequencies, the exponentials could underflow or overflow and cause problems. However, even in single precision, there is sufficient dynamic range and precision for the calculations presented here.

Once the eigenvalues are obtained, the homogeneous set of equations can be solved for each eigenvalue to obtain the coefficients. In our calculations, we set one of the coefficients (A_1) to unity, eliminated one of the equations [the second row in Eq. (A12)], and solved the reduced set of equations for the coefficients in terms of the one set to unity. The exact boundary conditions for the bottom half-space are used to avoid problems with growing exponentials. The LINPACK routines SGBFA and SGBSL are used to calculate the solutions. The value of the mode function at the ocean surface gives a measure of the accuracy of the solutions; the value of the normalized mode function is typically 10^{-6} for calculations performed on a DEC-20 computer in single (about eight digits) precision.

The relative values of the coefficients A_1, B_1, etc., are determined from the solution of the homogeneous equations given above in Eq. (A12). The absolute values of the coefficients are obtained by setting the normalization integral I_n equal to unity, where

$$I_n = \int_0^\infty \rho(Q_n^2 + P_n v_n) dz, \tag{A13}$$

with $Q_n = u_n + v_n'$, and $P_n = 2Q_n' + \kappa_s^2 v_n$. The mode attenuation coefficients δ_n and group velocities g_n are given by the formulas (Koch *et al.*, 1983):

$$\delta_n = (I_n \kappa_n)^{-1} \int_0^\infty \rho\{\varepsilon_p \kappa_p u_n^2 + \varepsilon_s \kappa_n^2 \kappa_s^{-3} \times [P_n^2 + 2Q_n(P_n' + \kappa_s^2 v_n')]\} dz, \quad (A14)$$

and

$$(g_n)^{-1} = (\omega I_n \kappa_n)^{-1} \int_0^\infty \rho\{\kappa_p^2 u_n^2 + \kappa_n^2 \kappa_s^{-2} \times [P_n^2 + 2Q_n(P_n' + \kappa_s^2 v_n')]\} dz. \quad (A15)$$

In our case, all the integrals can be computed analytically within each layer.

The solution is now complete. Propagation loss calculations for a source at depth z_0 in the water column are given by the usual expression 20 log$|P(r,z)|$, where

$$P(r,z) = i\pi\rho \sum_{n=0}^{N} u_n(z_0) u_n(z) H_0^{(1)}(\kappa_n r). \quad (A16)$$

The mode functions can also be summed incoherently, giving a smooth function of propagation loss versus range; this is quite useful when comparing propagation losses as a function of frequency, as in many of the figures in this paper. The SAFARI predictions had to smoothed by averaging over range in order to present easily interpreted results.

APPENDIX B: REFLECTION LOSS CALCULATIONS

Here, we outline the method used to calculate theoretical bottom reflection loss for the two-layer seabed model: a semi-infinite layer of water overlaying a thin layer of sediment (thickness d) and a semi-infinite hard-rock substrate. The equations are based on Brekhovskikh's calculations of the reflection and transmission coefficients for multilayered solid media (Brekhovskikh, 1980). We have extended that work to include the effect of absorption in the media, and also to permit calculation of the components of bottom reflection loss due to attenuation of compressional waves and shear waves in the thin layer of sediment. The effect of absorption in the media is included by using the following for the wavenumber:

$$\kappa = (\omega/c)(1 + i\varepsilon \ln 10/40\pi), \quad (B1)$$

where κ is the wavenumber including the effect of absorption in the media, ω is the angular frequency of the incident acoustic pressure wave, c is the sound speed in the medium, and ε is the absorption coefficient for the medium (dB/wavelength). The absorption coefficient, ε (dB/wavelength), may be calculated from the attenuation coefficients (in dB/m/kHz) given in the geoacoustic models by multiplying the attenuation coefficient by the sound speed, in meters per second, and dividing by 1000.

The reflection coefficient R_w for an acoustic wave incident on the seabed is given by [Brekhovskikh, 1980, Eq. (8.41)]

$$R_w = (Z_{\text{in}} - Z_w)/(Z_{\text{in}} + Z_w), \quad (B2)$$

where Z_{in} is the input impedance of the seabed [Brekhovskikh, 1980, Eq. (8.43)], $Z_w = \rho_w c_w / \sin(\theta_w)$ is the acoustic impedance of the water, and θ_w is the grazing angle of the incident wave. We have used the subscript w to refer to properties of the water layer. The bottom reflection loss, BL_w, is then given by

$$\text{BL}_w = -20 \log |R_w|. \quad (B3)$$

The components of bottom reflection loss due to the excitation of compressional and shear waves in the substrate and due to the absorption of compressional and shear waves in the sediment layer may be determined via calculations of energy flux. The energy flux vector, **E**, of any wave in the sediment layer or in the substrate is given by (Auld, 1973)

$$\mathbf{E} = -1/2 \,\text{Re}(\mathbf{v}^* \cdot \mathscr{T}), \quad (B4)$$

where $\mathbf{v}^*$ is the complex conjugate of the particle velocity vector, and $\mathscr{T}$ is the stress tensor.

The energy flux vector **E** can be regarded as the vector sum of a horizontal component parallel to plane-parallel media boundaries, and a vertical component normal to the boundaries. As we are primarily interested in energy passing from one medium to another across the plane boundary separating them, we will only consider the vertical component of the energy flux in what follows.

The ratio of reflected to incident vertical energy flux in the water layer is just the square of the reflection coefficient $|R_w|^2$, so by examining the vertical energy flux in the sediment and substrate layers, we can identify the various contributions to bottom reflection loss: absorption of compressional and shear waves in the sediment, and radiation of compressional and shear waves in the substrate.

Energy flux in the substrate layer can be related to the transmission coefficients for compressional waves and shear waves. Dividing the energy flux in the substrate by the energy flux in the water gives the relative energy flux in the substrate:

$$\text{RE}_{ps} = \{\rho_s \text{Re}[\kappa_{ps} \sin(\theta_{ps})]/\rho_w \kappa_w \sin(\theta_w)\} |T_p|^2, \quad (B5)$$

$$\text{RE}_{ss} = \{\rho_s \text{Re}[\kappa_{ss} \sin(\theta_{ss})]/\rho_w \kappa_w \sin(\theta_w)\} |T_s|^2, \quad (B6)$$

where RE_{ps} and RE_{ss} are the relative energy flux terms for the compressional and shear waves in the substrate, ρ_w and ρ_s are the density of water and the substrate material, κ are the wavenumbers, and θ are the grazing angles for the respective waves in the water and in the substrate. The transmission coefficients T_p and T_s of the velocity potentials for compressional and shear waves in the substrate are given by [Brekhovskikh, 1980, Eqs. (8.45) and (8.44)]

$$T_p = [(2Z_w)/Z_{\text{in}} + Z_w)]S \quad (B8)$$

and

$$T_s = G\, T_p, \quad (B7)$$

where S and G are nontrivial functions given by Brekhovskikh's Eqs. (8.46) and (8.44). The bottom loss components due to excitation of compressional and shear waves in the substrate are given by

$$\text{BL}_{ps} = -10 \log|1 - \text{RE}_{ps}| \quad (B9)$$

$$\text{BL}_{ss} = -10 \log|1 - \text{RE}_{ss}| \quad (B10)$$

Calculation of the components of bottom reflection loss due to absorption of compressional and shear waves in the thin layer of sediment is more involved. The energy absorbed in the layer may be found by calculating the energy flux at the top of the layer and subtracting the energy flux at the bottom. The difference may be taken to be the energy lost to absorption. The energy flux in the layer can be written in terms of potential functions associated with upward and downward traveling compressional and shear waves in the layer. We have, after some tedious calculations,

$$\begin{aligned} E_{pl}(z) = {} & 1/2\rho_l\omega\,\mathrm{Re}[\alpha]\,[\,|\phi_\mathrm{d}|^2\exp(2\,\mathrm{Im}[\alpha]z) \\ & - |\phi_\mathrm{u}|^2\exp(-2\,\mathrm{Im}[\alpha]z)\,] \\ & + \rho_l\omega\,\mathrm{Im}[\alpha]\mathrm{Im}[\phi_\mathrm{u}(\phi_\mathrm{d})^*\exp(2i\,\mathrm{Re}[\alpha]z)], \end{aligned} \tag{B11}$$

$$\begin{aligned} E_{sl}(z) = {} & 1/2\rho_l\omega\,\mathrm{Re}[\beta\,]\,[\,|\psi_\mathrm{d}|^2\exp(2\,\mathrm{Im}[\beta\,]z) \\ & - |\psi_\mathrm{u}|^2\exp(-2\,\mathrm{Im}[\beta\,]z)\,] \\ & + \rho_l\omega\,\mathrm{Im}[\beta\,]\,\mathrm{Im}[\psi_\mathrm{u}(\psi_\mathrm{d})^*\exp(2i\,\mathrm{Re}[\beta\,]z)], \end{aligned} \tag{B12}$$

where $E_{pl}(z)$ and $E_{sl}(z)$ are the compressional and shear-wave energy flux terms as functions of depth z in the sediment layer ($z=0$ at the boundary between the sediment layer and the substrate, $z=d$ at the boundary between the water and the sediment layer). The upward and downward traveling scalar and vector potentials are ϕ_u, ϕ_d, ψ_u, and ψ_d, respectively, ρ_l is the density of the sediment material, $\alpha = \kappa_{pl}\sin(\theta_{pl})$, and $\beta = \kappa_{sl}\sin(\theta_{sl})$.

The horizontal (x) and vertical (z) components of the particle displacement vector ($\mathbf{u}$) and the z-component of the stress tensor ($\mathscr{T}$) can be related to the scalar potential functions, ϕ_u and ϕ_d, associated with the compressional wave, and the vector potential functions, ψ_u and ψ_d, associated with the shear wave. This relationship is given by [Brekhovskikh, 1980, Eq. (8.26)]

$$\begin{bmatrix} u_x \\ u_z \\ \mathscr{T}_{zz} \\ \mathscr{T}_{xz} \end{bmatrix} = \mathbf{M}\begin{bmatrix} \phi_u + \phi_d \\ \phi_u - \phi_d \\ \psi_u - \psi_d \\ \psi_u + \psi_d \end{bmatrix}, \tag{B13}$$

where $\mathbf{M}$ is the 4×4 matrix given in Brekhovskikh's Eq. (8.26).

It is possible, in the case of a single layer, to invert the matrix $\mathbf{M}$, apply the necessary conditions of continuity at the interface with the substrate, and derive analytic expressions for the sums and differences of the potential functions. This work is straightforward but tedious, and will not be shown here. The bottom loss components due to compressional wave absorption, BL_{pl}, and shear-wave absorption, BL_{sl}, in the layer are then given by

$$\mathrm{BL}_{pl} = -10\log\left|1 - \frac{E_{pl}(d) - E_{pl}(0)}{1/2\rho_w\kappa_w\sin(\theta_w)}\right|, \tag{B14}$$

$$\mathrm{BL}_{sl} = -10\log\left|1 - \frac{E_{sl}(d) - E_{sl}(0)}{1/2\rho_w\kappa_w\sin(\theta_w)}\right|, \tag{B15}$$

In the absence of absorption within the sediment layer, the vertical energy flux at the top and the bottom of the layer should be the same, i.e., what goes in must come out. In Eqs. (B11) and (B12), the energy-flux components become independent of depth z, if $\mathrm{Im}[\alpha] = \mathrm{Im}[\beta] = 0$. (It is the imaginary part of the wavenumber that is associated with attenuation.) The contribution to the bottom loss from this layer is the difference in flux between the top and the bottom of the layer, so clearly it is the absorption of the waves in this layer that is important. In contrast, the primary contribution to the bottom loss from the substrate is due to radiation of energy away from the boundary, and absorption of those waves plays only a minor role.

ACKNOWLEDGMENTS

The SAFARI fast-field program was provided by SACLANT Undersea Research Centre. Much of the normal-mode code was developed by Jamie McLaren, a co-op student from the Department of Mathematics, Statistics, and Computing Science, Dalhousie University, Halifax, Nova Scotia.

Akal, T., and Jensen, F. B. (**1983**). "Effects of the sea-bed on acoustic propagation," in *Acoustics and the Sea-Bed*, edited by N. G. Pace (Bath, U. P., Bath, UK), pp. 225–232.

Auld, B. A. (**1973**). *Acoustic Fields and Waves in Solids, Vol. 1* (Wiley, New York), pp. 145.

Beebe, J. H., and Holland, C. W. (**1986**). "Shallow-water propagation effects over a complex, high-velocity bottom," J. Acoust. Soc. Am. **80**, 244–250.

Beebe, J. H. (**1980**). "Long-range propagation over a mixed-sediment, sloping bottom," J. Acoust. Soc. Am. Suppl. 1, **67**, S30.

Berkson, J. M., and Matthews, J. E. (**1983**). "Statistical properties of seafloor roughness," in *Acoustics and the Sea-Bed*, edited by N. G. Pace (Bath U. P., Bath, UK), pp. 215–223.

Brekhovskikh, L. M. (**1980**). *Waves in Layered Media* (Academic, New York).

Chamuel, J. R., and Brooke, G. H. (**1988**). "Transient Scholte wave transmission along rough liquid–solid interfaces," J. Acoust. Soc. Am. **83**, 1336–1344.

Chapman, D. M. F., and Ellis, D. D. (**1980**). "Propagation modeling on the Scotian Shelf: The geo-acoustic model," in *Bottom-Interacting Ocean Acoustics*, edited by W. A. Kuperman and F. B. Jensen (Plenum, New York), pp. 525–539.

Chapman, D. M. F., and Ellis, D. D. (**1983**). "The group velocity of normal modes," J. Acoust. Soc. Am. **74**, 973–979.

Dodds, D. J. (**1980**). "Attenuation estimates from high resolution subbottom profiler echoes," in *Bottom-Interacting Ocean Acoustics*, edited by W. A. Kuperman and F. B. Jensen (Plenum, New York), pp. 173–191.

Dongarra, J. J., Moler, C. B., Bunch, J. R., and Stewart, G. W. (**1979**). *LINPACK Users' Guide* (SIAM, Philadelphia, PA), Chapter 2.

Ellis, D. D., and Chapman, D. M. F. (**1985**). "A simple shallow-water propagation model including shear wave effects," J. Acoust. Soc. Am. **78**, 2087–2095.

Hall, M., Gordon, D. F., and White, D. (**1983**). "Improved methods for determining eigenfunctions in multilayered normal mode problems," J. Acoust. Soc. Am. **73**, 153–162.

Hamilton, E. L. (**1980**). "Geoacoustic modeling of the sea floor," J. Acoust. Soc. Am. **68**, 1313–1340.

Harrison, C. H., and Cousins, P. L. (**1985**). "A study of propagation loss dependence on sediment layer thickness using the Fast Field Program," in *Proceedings of Ocean Seismo-Acoustics: Low-Frequency Underwater Acoustics*, edited by T. Akal and J. M. Berkson (Plenum, New York), pp. 139–148.

IMSL Library User's Manual (**1982**). (IMSL Inc., Houston, Texas) ed. 9.

Koch, R. A., Penland, C., Vidmar, P. J., and Hawker, K. E. (**1983**). "On the calculation of normal mode group velocity and attenuation," J. Acoust. Soc. Am. **73**, 820–825.

Kuperman, W. A., and Schmidt, H. (**1986**). "Rough surface elastic wave scattering in a horizontally stratified ocean," J. Acoust. Soc. Am. **79**, 1767–1777.

MacPherson, J. D., and Fothergill, N. O. (**1962**). "Study of low-frequency sound propagation in the Hartlen Point region of the Scotian Shelf," J. Acoust. Soc. Am. **34**, 967–971.

Ozard, J. (**1989**). Personal communication, February, 1989, Defence Research Establishment Pacific, Victoria, B. C.

Schmidt, H. (**1988**). "SAFARI: Seismo-Acoustic Fast field Algorithm for

Range-Independent environments, User's Guide," SACLANT Undersea Research Centre Rep. SR-113, September 1988.

Staal, P. R. (**1987**). "Use and evolution of a modular digital hydrophone array," in *Proceedings of IEEE Oceans '87 Vol. I*, IEEE Cat. No. 87-CH2498-4, pp. 161–166.

Staal, P. R. (**1983**). "Acoustic propagation measurements with a bottom-mounted array," in *Acoustics and Sea-Bed*, edited by N. G. Pace (Bath U. P., Bath, UK), pp. 289–296.

Staal, P. R. and Chapman, D. M. F. (**1985**). "Observations of interface waves and low-frequency acoustic propagation over a rough granite seabed," in *Proceedings of Ocean Seismo-Acoustics: Low-Frequency Underwater Acoustics*, edited by T. Akal and J. M. Berkson (Plenum, New York), pp. 643–652.

Staal, P. R., Chapman, D. M. F., and Zakarauskas, P. (**1986**). "The effect of variable roughness of a granite seabed on low-frequency shallow-water acoustic propagation," in *Progress in Underwater Acoustics*, edited by H. M. Merklinger (Plenum, New York), pp. 485–492.

Urick, R. J. (**1975**). *Principles of Underwater Sound for Engineers* (McGraw-Hill, New York), p. 161.

Vidmar, P. J. (**1980a**). "The effect of sediment rigidity on bottom reflection loss in a typical deep sea sediment," J. Acoust. Soc. Am. **68**, 634–638.

Vidmar, P. J. (**1980b**). "Ray path analysis of sediment shear wave effects on bottom reflection loss," J. Acoust. Soc. Am. **68**, 639–648.

Worley, R. D., and Walker, R. A. (**1982**). "Low-frequency ambient ocean noise and sound transmission over a thinly sedimented rock bottom," J. Acoust. Soc. Am. **71**, 863–870.